Estimation of Residual Motion Errors in Airborne SAR Interferometry Based on Time-Domain Backprojection and Multisquint Techniques

Ning Cao, Hyongki Lee, Evan Zaugg, Ramesh Shrestha, William E. Carter, Craig Glennie, Zhong Lu, and Hanwen Yu

***Abstract*— For airborne repeat-pass synthetic aperture radar interferometry (InSAR), precise trajectory information is needed to compensate for deviations of the platform movement from a linear track. Using the trajectory information, motion compensation (MoCo) can be implemented within SAR data focusing. Due to the inaccuracy of current navigation systems, residual motion errors (RMEs) exist between the real and measured trajectory, causing phase undulations in the final interferograms. Up to now, MoCo and RME estimation have usually been combined in airborne InSAR to estimate ground deformation. Conventional MoCo methods generally involve azimuthal and range resampling and phase correction. Then frequency-domain focusing techniques can be used to generate the SAR images. After focusing SAR images with MoCo, both multisquint and autofocus approaches can be used to estimate RME. In addition to the MoCo-based frequency-domain focusing, the time-domain backprojection (BP) technique can also focus the SAR data obtained from highly nonlinear platform trajectories. In this paper, we present, for the first time, the combination of BP and multisquint techniques for RME estimation. A detailed derivation of the implementation of the multisquint approach using the BP-focusing images is presented. Repeat-pass data from the SlimSAR system over Slumgullion landslide are used to demonstrate the feasibility of RME estimation for both stationary and nonstationary scenes. We conclude that the proposed method can effectively remove the RME.**

***Index Terms*— Backprojection (BP), motion compensation (MoCo), residual motion error (RME), SAR interferometry (InSAR), synthetic aperture radar (SAR).**

I. Introduction

AMONG the various remote-sensing techniques, synthetic aperture radar interferometry (InSAR) has proven to be a powerful tool for measuring ground deformation with millimeter- to centimeter-scale accuracy [1], [2]. In comparison with the spaceborne SAR, airborne SAR systems have the advantages of flexible scanning geometry and revisit times, easy to maintain and update, and no ionospheric distortion. Therefore, we hypothesize that the routine use of airborne InSAR could greatly expand access to observational data for researchers to better characterize, quantify, and understand the behavior of many natural hazards [3]. However, only a few airborne SAR systems have been successfully deployed for deformation mapping through repeat-pass interferometry, such as the E-SAR (and its successor F-SAR) system from the German Aerospace Center [4], UAVSAR from the Jet Propulsion Laboratory [5], and OrbiSAR from OrbiSat [6]. The major challenge of airborne InSAR for deformation mapping is correcting the observations for deviations in the trajectories estimated by a combination of Global Navigation Satellite System (GNSS) and Inertial Measurement Unit (IMU) observations. Using the trajectory information, motion compensation (MoCo) can be implemented in SAR data processing [7]. The basic procedure of MoCo is to: 1) generate a linear reference trajectory that best fits the actual trajectory; 2) calculate the offset between the reference trajectory and measured trajectory; and 3) apply motion corrections by interpolation and phase compensation. It is also necessary to use an external digital elevation model (DEM) in the MoCo procedure to make topography-dependent phase corrections [8]–[11].

Even after applying MoCo, errors in the trajectory estimated from the GNSS/IMU system, referred to as residual motion errors (RMEs), still exist. The RME can cause erroneous phase undulations in the final interferogram. Recent GNSS/IMU navigation systems can determine the aircraft trajectories with an estimated precision of 1–10 cm [15], [16]. In recent years, several advanced algorithms have attempted to estimate and remove the RME [12]–[17]. For example, in [12]–[16], multisquint techniques were used to estimate RME from the registration error. Through an aperture splitting procedure, SAR images with different squint angles can be obtained, and the corresponding interferograms can be generated. Then, the residual baseline errors can be estimated from the phase differences between the interferograms. In addition to the multisquint methods, advanced autofocus algorithms have also been proposed to compensate for RME [17].

In practice, RME estimation is combined with the MoCo procedure to obtain reliable interferograms. In addition to the MoCo methods mentioned previously, the time-domain backprojection (BP) technique can also focus the SAR data

Manuscript received August 21, 2017; revised October 23, 2017; accepted November 29, 2017. Date of publication December 29, 2017; date of current version March 23, 2018. This work was supported by the National Center for Airborne Laser Mapping under Project NSF EAR-1043051. *(Corresponding author: Hyongki Lee.)*

N. Cao, H. Lee, R. Shrestha, W. E. Carter, C. Glennie, and H. Yu are with the Department of Civil and Environmental Engineering, University of Houston, Houston, TX 77204-4003 USA, and also with the National Center for Airborne Laser Mapping, University of Houston, Houston, TX 77204-5059 USA (e-mail: ncao5@uh.edu; hlee@uh.edu).

E. Zaugg is with ARTEMIS, Inc., Hauppauge, NY 11788 USA.

Z. Lu is with the Roy M. Huffington Department of Earth Sciences, Southern Methodist University, Dallas, TX 75205 USA.

Color versions of one or more of the figures in this paper are available online at http://ieeexplore.ieee.org.

Digital Object Identifier 10.1109/TGRS.2017.2779852

obtained from nonlinear platform trajectories [19]–[24]. Unlike the frequency-domain SAR image formation techniques, the time-domain BP method requires trajectory data as well as a reconstruction-grid (such as a DEM) to be known [23], [24]. Compared with frequency-domain focusing, the time-domain BP method has the advantages of: 1) being simple and straightforward; 2) focusing the data obtained from significantly nonlinear trajectories, which is common for airborne platforms (i.e., topography- and aperture-dependent MoCo is inherently taken into account); and 3) focusing the data directly on the desired reconstruction grid thus avoiding the need for geocoding [25]. The major drawback of the BP algorithm is its heavy computational burden, which can be mitigated by employing the fast-factorized BP method [22]. Until now, no study has investigated the use of the BP-based method to estimate RME for the purpose of deformation mapping. Therefore, in this paper, a time-domain RME estimation algorithm is proposed for airborne InSAR data by combining the BP focusing and multisquint RME estimation techniques.

The major advantage of the proposed BP-based RME estimation method is that BP-based methods are more suitable to process airborne SAR data obtained with highly nonlinear flight tracks [23], [24]. The trajectories of such small aircrafts depend on factors, including rugged terrain, atmospheric turbulence, and curvilinear areas of interest, such as traffic routes, pipelines, and rivers. In such scenarios, acquiring SAR data along a nonlinear trajectory would be more cost-effective and time-saving compared with repeatedly flying linear tracks to cover the area of interest. Even though a patchwise frequency-domain focusing and mosaicking technique can be used to process SAR data obtained from highly nonlinear flight tracks, the patchwise processing method is limited and insufficient as discussed in [23]. Therefore, the study of BP-based RME estimation is needed to process such repeat-pass InSAR data obtained with highly nonlinear flight tracks, especially from small aircraft flying at low altitude.

This paper is organized as follows. A detailed description of the BP focusing algorithm and BP-based RME estimation method is given in Section II. Section III provides the experimental results to verify RME removal capabilities for both stationary and nonstationary scenes. Finally, we conclude with Section IV which summarizes our results.

II. Algorithm

A. Signal Analysis of the BP Focusing Technology

A brief derivation of the time-domain BP algorithm for a point target is given in this section. The transmitted signal of the radar is normally a "chirp" (linear frequency-modulated signal). For simplicity, the following analysis is based on stop-go approximation, i.e., the antenna remains at the same location during the transmitting and receiving of one pulse. Under the stop–go approximation, the SAR focusing can be broken into two separate steps (range and azimuth compressions). After demodulation and range-compression, the range-compressed signal can be given by

$$s_{RC}(i) = A_i \exp\{-j2\pi f_0 \tau_i\} \tag{1}$$

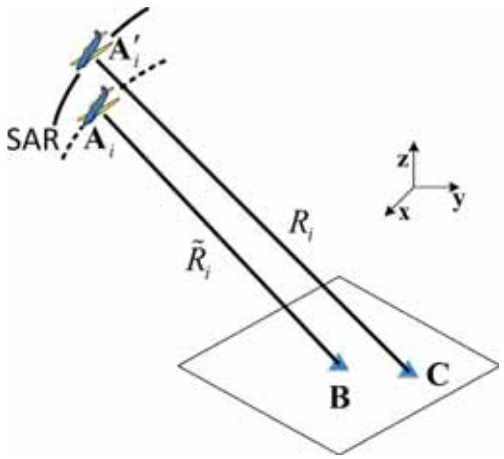

Fig. 1. SAR scanning geometry for a single pixel. Points $\mathbf{A}_i$, $\mathbf{A}_i'$, $\mathbf{B}$, and $\mathbf{C}$ are the measured position of the SAR antenna, true position of the SAR antenna, physical center of the cell, and actual phase center of a scattering target, respectively.

where i is the slow-time pulse index, A_i is the amplitude, f_0 is the center frequency, and τ_i is the two-way propagation time from the radar antenna to the target. Assuming that R_i is the real range from the true radar antenna position to the phase center of a target, we have $\tau_i = 2R_i/c$. An important step for the BP algorithm is to compensate the phase component in (1) using the estimated two-way propagation time $\tilde{\tau}_i$. Here, $\tilde{\tau}_i$ can be estimated from $\tilde{\tau}_i = 2\tilde{R}_i/c$, where $\tilde{R}_i$ is the estimated radar-target range from the radar position to the physical center of a scattering cell. In general, the target is assumed to be located at the center of the cell. Therefore, as shown in Fig. 1, $\tilde{R}_i$ can be estimated from the SAR scanning geometry using the trajectory information and specified reconstruction grid. It should be noted that the physical center of the cell represents the estimated phase center of the target, since the exact phase center of the target is unknown. Then, we obtain the phase-compensated signal $s_{RC}^{\text{comp}}(i)$ as

$$\begin{aligned} s_{RC}^{\text{comp}}(i) &= s_{RC}(i) \exp\{j2\pi f_0 \tilde{\tau}_i\} \\ &= A_i \exp\{-j2\pi f_0 (2R_i/c - 2\tilde{R}_i/c)\} \\ &= A_i \exp\{-jk\Delta R_i\} \end{aligned} \tag{2}$$

where $k = 4\pi/\lambda$ and $\Delta R_i = R_i - \tilde{R}_i$. λ is the wavelength. It should be noted that a range migration correction procedure is not needed in the BP algorithm, because the range values can be directly estimated from the trajectory data and the reconstruction grid. A basic BP process is to coherently integrate the phase-compensated range-compressed radar echoes $s_{RC}^{\text{comp}}(i)$ to form the image. For a point target, the backprojected signal is

$$I_{\text{BP}} = \sum_{i=-N}^{M} s_{RC}^{\text{comp}}(i) = \sum_{i=-N}^{M} A_i \exp\{-jk\Delta R_i\}. \tag{3}$$

Here, i is assumed to vary from $-N$ to M during the integration along the azimuth. $-N$ and M represent the range of the azimuth pulse index, which can be determined from the used aperture length. For a system with zero squint angle, we have $N = M$. Therefore, we can see that the backprojected signal I_{BP} contains the "residual phase" caused by the range difference ΔR_i [24]. The range difference ΔR_i has two

components: the offset between the measured antenna position and the true antenna position; and the offset between the physical center and phase center of a scattering cell. In order to further study the properties of the BP algorithm, a detailed analysis of this "residual phase" is needed.

For further analysis, the coordinates of Points $\mathbf{A}_i$, $\mathbf{A}_i'$, $\mathbf{B}$, and $\mathbf{C}$ in Fig. 1 are set to $(x_{i,A}, y_{i,A}, z_{i,A})$, $(x'_{i,A}, y'_{i,A}, z'_{i,A})$, (x_B, y_B, z_B), and (x_C, y_C, z_C), respectively. Assuming $\boldsymbol{\varepsilon}(\varepsilon_x, \varepsilon_y, \varepsilon_z) = \mathbf{C} - \mathbf{B}$ and $\boldsymbol{\sigma}_i(\sigma_{i,x}, \sigma_{i,y}, \sigma_{i,z}) = \mathbf{A}_i' - \mathbf{A}_i$, the off range R_i and $\tilde{R}_i$ can be expressed as [24], [32]

$$\begin{aligned}\tilde{R}_i &= \|\mathbf{A}_i - \mathbf{B}\| = \sqrt{(x_{i,A}-x_B)^2 + (y_{i,A}-y_B)^2 + (z_{i,A}-z_B)^2} \\ R_i &= \left\|\mathbf{A}_i' - \mathbf{C}\right\| = \|\mathbf{A}_i - \mathbf{B} - (\boldsymbol{\varepsilon} - \boldsymbol{\sigma}_i)\| \\ &\approx \tilde{R}_i - \frac{(\mathbf{A}_i - \mathbf{B}) \cdot (\boldsymbol{\varepsilon} - \boldsymbol{\sigma}_i)}{\|\mathbf{A}_i - \mathbf{B}\|}. \end{aligned} \tag{4}$$

Therefore, the range difference ΔR_i can be estimated from (4) as

$$\Delta R_i = R_i - \tilde{R}_i \approx \frac{(\mathbf{B} - \mathbf{A}_i) \cdot (\boldsymbol{\varepsilon} - \boldsymbol{\sigma}_i)}{\|\mathbf{B} - \mathbf{A}_i\|} = \boldsymbol{\mu}_i \cdot (\boldsymbol{\varepsilon} - \boldsymbol{\sigma}_i) \tag{5}$$

where $\boldsymbol{\mu}_i = ((\mathbf{B} - \mathbf{A}_i)/(\|\mathbf{B} - \mathbf{A}_i\|))$ is the unitary vector from Point $\mathbf{A}_i$ to Point $\mathbf{B}$. Therefore, we can see that the range difference ΔR_i can be estimated by the length of the component of vector $\boldsymbol{\varepsilon} - \boldsymbol{\sigma}_i$ in the instantaneous $\mathbf{A}_i\mathbf{B}$ direction during scanning. The approximation in (5) is valid, since vector $\mathbf{A}_i\mathbf{B}$ and vector $\mathbf{A}_i'\mathbf{C}$ can be assumed to be parallel. Since vector $\boldsymbol{\varepsilon} - \boldsymbol{\sigma}_i$ is not in the slant-range and along-track plane like vector $\mathbf{A}_i\mathbf{B}$, only the partial component of vector $\boldsymbol{\varepsilon} - \boldsymbol{\sigma}_i$ in this plane can make a contribution to the range difference in (5). Therefore, we assume the components of vectors $\boldsymbol{\varepsilon}$ and $\boldsymbol{\sigma}_i$ in the slant-range and along-track planes are $\boldsymbol{\varepsilon}'$ and $\boldsymbol{\sigma}_i'$, respectively. Therefore, we have $\boldsymbol{\mu}_i \cdot (\boldsymbol{\varepsilon} - \boldsymbol{\sigma}_i) = \boldsymbol{\mu}_i \cdot (\boldsymbol{\varepsilon}' - \boldsymbol{\sigma}_i')$. Due to the aircraft motion, the slant-range and along-track planes here mean the averaged slant-range and along-track plane during the scanning, respectively (when i changes from $-N$ to M).

We further decompose the offset vectors $\boldsymbol{\varepsilon}'$ and $\boldsymbol{\sigma}_i'$ into the slant-range and along-track directions as $\boldsymbol{\varepsilon}' = \boldsymbol{\varepsilon}_r + \boldsymbol{\varepsilon}_a$ and $\boldsymbol{\sigma}_i' = \boldsymbol{\sigma}_{i,r} + \boldsymbol{\sigma}_{i,a}$, respectively. As shown in Fig. 2, (5) can be rewritten as

$$\begin{aligned}\Delta R_i &= \boldsymbol{\mu}_i \cdot (\boldsymbol{\varepsilon} - \boldsymbol{\sigma}_i) = \boldsymbol{\mu}_i \cdot \left(\boldsymbol{\varepsilon}' - \boldsymbol{\sigma}_i'\right) \\ &= \boldsymbol{\mu}_i \cdot (\boldsymbol{\varepsilon}_r - \boldsymbol{\sigma}_{i,r} + \boldsymbol{\varepsilon}_a - \boldsymbol{\sigma}_{i,a}) \\ &= (\varepsilon_r - \sigma_{i,r}) \cos\alpha_i + (\varepsilon_a - \sigma_{i,a}) \sin\alpha_i \end{aligned} \tag{6}$$

where α_i is the angle between vector $\mathbf{A}_i\mathbf{B}$ and the slant-range direction. It should be noted that the slant-range direction here is the slant range direction at zero Doppler time. During scanning, vector $\mathbf{A}_i\mathbf{B}$ can be regarded as the instantaneous line of sight (LOS) direction. Consequently, α_i can be regarded as the instantaneous squint angle. Substituting (6) into (2), we can obtain

$$\begin{aligned}s_{RC}^{\text{comp}}(i) &= A_i \exp\{-jk(\varepsilon_r - \sigma_{i,r})\cos\alpha_i - jk(\varepsilon_a - \sigma_{i,a})\sin\alpha_i\} \\ &\approx A_i \exp\{-jk(\varepsilon_r - \sigma_{i,r}) - jk(\varepsilon_a - \sigma_{i,a})\alpha_i\}. \end{aligned} \tag{7}$$

Since α_i is generally very small ($<2°\sim5°$ for airborne SAR and $<3\times10^{-6}°$ for spaceborne SAR), we have $\cos\alpha_i \approx 1$ and $\sin\alpha_i \approx \alpha_i$. Consequently, α_i can be seen as a linear function of i. Therefore, (3) becomes

$$I_{\text{BP}} \approx \sum_{i=-N}^{M} A_i \exp\{-jk(\varepsilon_r - \sigma_{i,r}) - jk(\varepsilon_a - \sigma_{i,a})\alpha_i\}. \tag{8}$$

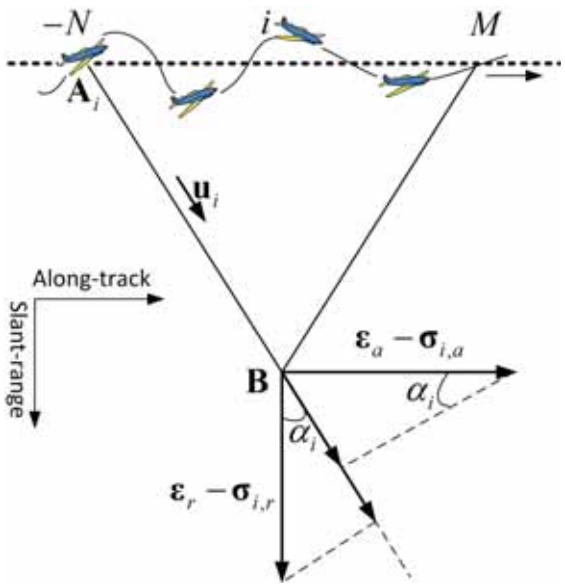

Fig. 2. Decomposition of the offset vector $\boldsymbol{\varepsilon}' - \boldsymbol{\sigma}_i'$ into slant-range and along-track directions.

In order to analyze the effect of the RME on the backprojected signal I_{BP}, four scenarios can be considered as in the following. For simplification, we assume that the system squint angle is zero ($M = N$) and the response of the target is symmetric with respect to $i = 0$ (i.e., $A_i \approx A_{-i}$ and $\alpha_i = -\alpha_{-i}$). Moreover, because phase component $k\sigma_{i,a}\alpha_i$ in (8) tends to be much smaller than the other terms, we can safely assume that RME mainly comes from the range error instead of the azimuth error (i.e., $\sigma_{i,a} \approx 0$).

Case 1 (No RME, i.e., $\sigma_{i,r} = 0$): If no RME exists, (8) can be rewritten as

$$\begin{aligned}I_{\text{BP}} &= A_0 \exp\{-jk\varepsilon_r\} + \sum_{i=1}^{N} (A_i \exp\{-jk\varepsilon_r\} \cdot 2\cos(k\varepsilon_a\alpha_i)) \\ &= A_0 \exp\{-jk\varepsilon_r\} + \sum_{i=1}^{N} \left(A_i' \exp\{-jk\varepsilon_r\}\right) \end{aligned} \tag{9}$$

where $A_i' = 2A_i \cos(k\varepsilon_a\alpha_i)$. From (9), it can be seen that the essence of the BP algorithm is a coherent summation procedure. The BP algorithm also only contains the information for the range offset ε_r. Therefore, the backprojected signal I_{BP} for a scattering cell has the form

$$I_{\text{BP}} \approx |I_{\text{BP}}| \exp\{-jk\varepsilon_r\}. \tag{10}$$

It is known that the azimuth-compressed signal for one target in the frequency domain has the following form:

$$I_{\text{Freq}} \approx |I_{\text{Freq}}| \exp\{-jkR_0\} \tag{11}$$

where R_0 is the shortest range from the antenna to the target at time $i = 0$, in which case $\Delta R_0 = R_0 - \tilde{R}_0 = \varepsilon_r$. The range

offset ε_r is caused by the noncompensated delay. It should be noted that the system squint angle is assumed to be zero and the slant-range direction here is the slant range direction at zero Doppler time. For the cases of nonzero Doppler centroid, a similar result can be obtained with R_0 corresponding to the sensor location where the target is illuminated with the peak antenna pattern. Since $\tilde{R}_0$ is known from the geometry, we can add back the phase component of $\tilde{R}_0$ into I_{BP} as

$$\begin{aligned} I_{\mathrm{BP}} \exp\{-jk\tilde{R}_0\} &= |I_{\mathrm{BP}}| \exp\{-jk(\varepsilon_r + \tilde{R}_0)\} \\ &= |I_{\mathrm{BP}}| \exp\{-jkR_0\}. \end{aligned} \tag{12}$$

Comparing (12) with (11), it can be seen that the BP algorithm obtains the same phase component as frequency-domain-focusing methods. Therefore, we can perform the SAR interferometry using the backprojected signal I_{BP}. In practice, it is not necessary to add back the phase component of $\tilde{R}_0$ into I_{BP}. The interferogram can be directly obtained by calculating the complex conjugate multiplication of the back-projected signals I_{BP} of the Master and Slave data. In other words, unlike frequency-domain interferometry, time-domain interferometry can be implemented without flattening and removal of topographic phase components. For clarification, in this paper, all the obtained single look complex (SLC) images were generated from signals I_{BP} without adding back the phase component of $\tilde{R}_0$. Therefore, the obtained interferograms do not contain topographic phase components. It should also be noted that the BP-focused images are inherently georegistered and projected onto the reconstruction grid [23], [25]. Instead of focusing the image onto the natural range/azimuth geometry of conventional SAR-focusing techniques, BP can directly focus the image onto a desired 3-D reconstruction-grid, which can be generated using an accurate DEM. Therefore, no geocoding is needed in the interferometry procedure.

In the BP method, the motion of the platform is compensated for by calculating the range $\tilde{R}_i$ and removing the corresponding phase component. In other words, the topography- and aperture-dependent MoCo is inherently applied to every individual target. Therefore, the BP technique can fully compensate for the aberrations caused by trajectory deviations, given precise antenna positions.

Case 2 (Constant RME, i.e., $\sigma_{i,r} = \sigma_r$): For constant RME, similar to (9) and (10), (8) can be rewritten as

$$I_{\mathrm{BP}} \approx |I_{\mathrm{BP}}| \exp\{-jk(\varepsilon_r - \sigma_r)\} \tag{13}$$

which means that a constant RME induces a phase offset directly related to the RME in range.

Case 3 (Linear RME, i.e., $\sigma_{i,r} = \sigma_r \alpha_i$):

$$\begin{aligned} I_{\mathrm{BP}} &\approx \sum_{i=-N}^{N} A_i \exp\{-jk(\varepsilon_r - \sigma_{i,r}) - jk\varepsilon_a \alpha_i\} \\ &= \sum_{i=-N}^{N} A_i \exp\{-jk\varepsilon_r - jk(\varepsilon_a - \sigma_r)\alpha_i\} \\ &= |I_{\mathrm{BP}}| \exp\{-jk\varepsilon_r\}. \end{aligned} \tag{14}$$

We can see from (14) that a linear RME does not induce a phase offset. Comparing (8) and (14), a linear RME $\sigma_r \alpha_i$ can shift the target impulse response by σ_r in the azimuth direction.

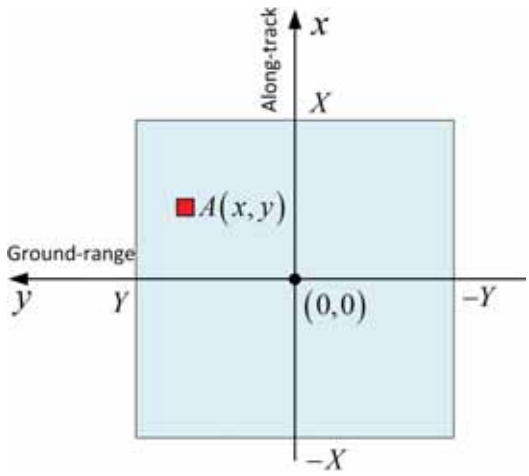

Fig. 3. Diagram of a distributed target centered at $(0, 0)$ with size of 2X and 2Y in along-track and ground-range directions, respectively. The red rectangle indicates a small scatterer with a complex response $A(x, y)$.

Case 4 (Quadratic RME, i.e., $\sigma_{i,r} = \sigma_r \alpha_i^2$):

$$\begin{aligned} I_{\mathrm{BP}} &\approx \sum_{i=-N}^{N} A_i \exp\left\{-jk\left(\varepsilon_r - \sigma_r \alpha_i^2\right) - jk\varepsilon_a \alpha_i\right\} \\ &= \sum_{i=-N}^{N} A_i \exp\left\{-jk\varepsilon_r - jk\varepsilon_a \alpha_i + jk\sigma_r \alpha_i^2\right\}. \end{aligned} \tag{15}$$

For quadratic and higher order RME, both defocusing and phase offset will occur due to the nonlinear phase component. From the above-mentioned analysis, we can see the effect of RME on BP focusing, and a constant RME causes a phase offset; a linear RME induces an azimuth shift of the target impulse response; and a quadratic (and higher order) RME can cause both defocusing and phase offsets. Similar conclusions have also been stated in the literature in the case of frequency-domain focusing [13], [26], which is expected, since time-domain BP focusing is theoretically equivalent to frequency-domain focusing techniques.

B. BP-Based RME Estimation

For simplification, the derivation in Section II-A has been based on analyzing the signal model of a point target. In order to implement the interferometry, it is necessary to consider a distributed target (DT). Fig. 3 shows a diagram of a DT. Corresponding to (7), the $s_{RC}^{\mathrm{comp}}(i)$ signal for this DT can be expressed as

$$\begin{aligned} s_{RC}^{\mathrm{comp}}(i) = \iint & A(x, y) W(x, y) \\ & \times \exp\left\{ \begin{matrix} -jk\varepsilon_r(x, y) - jk\varepsilon_a(x, y)\alpha_i \\ +jk(\sigma_{i,r} + \sigma_{i,a}\alpha_i) \end{matrix} \right\} dxdy. \end{aligned} \tag{16}$$

where $A(x, y)$ is the complex backscatter at each point on the ground, $W(x, y)$ is the system impulse response, and $\varepsilon_r(x, y)$ and $\varepsilon_a(x, y)$ are the offset functions (corresponding to ε_r and ε_a, respectively) in the slant-range and along-track

directions, respectively. Assuming that the incidence angle is θ and the physical center of the resolution cell is $(0, 0)$, it is straightforward to get the expressions for $\varepsilon_r(x, y)$ and $\varepsilon_a(x, y)$ from the imaging geometry as

$$\begin{cases} \varepsilon_r(x, y) = y \sin\theta \\ \varepsilon_a(x, y) = x. \end{cases} \tag{17}$$

Substituting (17) into (16), we have

$$s_{RC}^{\text{comp}}(i) = \iint A(x, y)W(x, y) \times \exp\left\{ \begin{matrix} -jky\sin\theta - jkx\alpha_i \\ +jk(\sigma_{i,r} + \sigma_{i,a}\alpha_i) \end{matrix} \right\} dxdy. \tag{18}$$

In order to estimate the RME using a multisquint methodology, SLC images with different subapertures are needed. Unlike splitting the aperture with azimuth band filtering in frequency-domain focusing, aperture splitting in time-domain BP can be obtained by splitting the integration procedure in azimuth. Without loss of generality, the SLC image focused by subaperture, indicated by i changing from n to m, can be obtained by

$$\begin{aligned} I_{\text{BP}} &= \sum_{i=n}^{m} s_{RC}^{\text{comp}}(i) \\ &= \sum_{i=n}^{m} \iint A(x, y)W(x, y) \exp\left\{ \begin{matrix} -jky\sin\theta \\ -jkx\alpha_i + jk\sigma_r \end{matrix} \right\} dxdy \\ &= \iint \alpha_{m-n} A(x, y)W(x, y) \exp\left\{ \begin{matrix} -jky\sin\theta \\ -jkx\alpha_{(m+n)/2} + jk\sigma_r \end{matrix} \right\} \\ &\quad \cdot \operatorname{sinc}(kx\alpha_{(m-n)/2}) dxdy \end{aligned} \tag{19}$$

where $\operatorname{sinc}(x) = \sin x/x$. The derivation of (19) assumes that RME only contains a constant value in range (i.e., $\sigma_{i,r} = \sigma$ and $\sigma_{i,a} = 0$) within the subaperture. In the following analysis, the constant parameter α_{m-n} in (19) is omitted. We can assume that the DT is initially centered at $(0, 0)$ and scanned by a Master flight. During a certain period of time, the DT has been displaced by $\Delta\varepsilon_r$ in the slant-range direction and $\Delta\varepsilon_a$ in the azimuth direction, and was scanned again by a Slave flight. For simplification, the following analysis assumes that the scattering property of the DT [i.e., $A(x, y)$] does not change during the time span between the Master and Slave scans. Based on (19), the focused signals for the Master and Slave flights for the same subaperture can be expressed as

$$\begin{cases} I_M = \iint A(x, y)W(x, y) \\ \quad \times \exp\{-jky\sin\theta_M - jkx\alpha_{(m+n)/2} + jk\sigma_M\} \\ \quad \cdot \operatorname{sinc}(kx\alpha_{(m-n)/2}) dxdy \\ I_S = \iint A(x, y)W(x, y) \\ \quad \times \exp\left\{ \begin{matrix} -jky\sin\theta_S - jk\Delta\varepsilon_r - jkx\alpha_{(m+n)/2} \\ -jk\Delta\varepsilon_a\alpha_{(m+n)/2} + jk\sigma_S \end{matrix} \right\} \\ \quad \cdot \operatorname{sinc}(kx\alpha_{(m-n)/2}) dxdy \end{cases} \tag{20}$$

where θ_M and θ_S are the incidence angles for Master and Slave flights, respectively, and σ_M and σ_S are the corresponding RMEs in the range direction. The interferometric phase can be estimated from the phase difference between I_M and I_S as

$$\begin{aligned} &\langle I_M \cdot I_S^* \rangle \\ &= \iiiint A(x, y)A^*(x', y')W(x, y)W^*(x', y') \\ &\quad \cdot \exp\left\{ \begin{matrix} -jky\sin\theta_M + jky'\sin\theta_S - jkx\alpha_{(m+n)/2} \\ +jkx'\alpha_{(m+n)/2} + jk\Delta\varepsilon_r + jk\Delta\varepsilon_a\alpha_{(m+n)/2} + jk\sigma_{M,S} \end{matrix} \right\} \\ &\quad \cdot \operatorname{sinc}(kx\alpha_{(m-n)/2}) \operatorname{sinc}(kx'\alpha_{(m-n)/2}) dxdydx'dy' \end{aligned} \tag{21}$$

where $\sigma_{M,S} = \sigma_M - \sigma_S$ is the RME difference between two acquisitions and $\langle\rangle$ represents the multilook procedure. It should be noted that RME correction technologies aim to estimate the differential RME $\sigma_{M,S}$ rather than the individual error of each acquisition. For simplification, we can assume that the small scatterers inside this DT are uniformly distributed and uncorrelated, which means [27]

$$\langle A(x, y)A^*(x', y') \rangle = C \cdot \delta(x - x', y - y') \tag{22}$$

where C is the average radar cross section. Substituting (22) into (21) gives

$$\begin{aligned} \langle I_M \cdot I_S^* \rangle &= C \cdot \exp\{jk\Delta\varepsilon_r + jk\Delta\varepsilon_a\alpha_{(m+n)/2} + jk\sigma_{\text{M,S}}\} \\ &\quad \cdot \iint |W(x, y)|^2 |\operatorname{sinc}(kx\alpha_{(m-n)/2})|^2 \\ &\quad \times \exp\{-jky\cos\theta\ \delta\theta\} dxdy \end{aligned} \tag{23}$$

where $\theta = ((\theta_M + \theta_S)/2)$ and $\delta\theta = \theta_M - \theta_S$. For a range-compressed signal, the impulse response can be approximated by

$$W(x, y) \approx \operatorname{sinc}\left(\frac{\pi y}{R_y}\right) \tag{24}$$

where R_y is the range resolution. Consequently, (23) becomes

$$\begin{aligned} \langle I_M \cdot I_S^* \rangle &= C \cdot \exp\{jk\Delta\varepsilon_r + jk\Delta\varepsilon_a\alpha_{(m+n)/2} + jk\sigma_{M,S}\} \\ &\quad \cdot \iint |\operatorname{sinc}(kx\alpha_{(m-n)/2})|^2 |\operatorname{sinc}(\pi y/R_y)|^2 \\ &\quad \times \exp\{-jky\cos\theta\delta\theta\} dxdy. \end{aligned} \tag{25}$$

The integration over y can be regarded as a Fourier kernel, which leads to the following expression after normalization:

$$\begin{aligned} \langle I_M \cdot I_S^* \rangle &= \left(1 - \frac{2\cos\theta|\delta\theta|R_y}{\lambda}\right) \\ &\quad \cdot \exp\{jk\Delta\varepsilon_r + jk\Delta\varepsilon_a\alpha_{(m+n)/2} + jk\sigma_{M,S}\}. \end{aligned} \tag{26}$$

Equation (26) gives the interferometry of Master and Slave scanning for subaperture $m \le i \le n$ with effective squint angle $\alpha_{(m+n)/2}$. It is easy to see that the interferometric phase contains components induced by range direction motion $\Delta\varepsilon_r$, along-track motion $\Delta\varepsilon_a$ weighted by effective squint angle, and RME difference $\sigma_{M,S}$ between Master and Slave scans. From (26), we can also obtain the spatial baseline decorrelation function as

$$\gamma_{\text{spatial,BP}} = 1 - \frac{2\cos\theta|\delta\theta|R_y}{\lambda}. \tag{27}$$

Equation (27) is identical to the decorrelation function given in [27]. Based on (26), in order to estimate the RME $\sigma_{M,S}$,

the differential phases for the two interferograms generated from the two subapertures can be obtained as

$$\dot{\Phi}^{s1,s2} = \Phi^{s1} - \Phi^{s2} = \arg\left\{\left\langle I_M^{s1} \cdot I_S^{s1*}\right\rangle \cdot \left\langle I_M^{s2} \cdot I_S^{s2*}\right\rangle^*\right\} = k(\Delta\varepsilon_a(\alpha_{s1} - \alpha_{s2}) + \sigma_{M,S}(s1) - \sigma_{M,S}(s2)) \quad (28)$$

where $s1$ and $s2$ denote two subapertures with effective squint angles α_{s1} and α_{s2}, respectively, and Φ^{s1} and Φ^{s2} represent the interferograms generated from subapertures $s1$ and $s2$, respectively. It should be noted that the differential phases are less sensitive to along-track motion $\Delta\varepsilon_a$ than the RME $\sigma_{M,S}$ due to the scale factor $\alpha_{s1} - \alpha_{s2}$. In other words, a short separation of subapertures can reduce the effect of along-track motion on the RME estimation. From (28), the RME estimation can be classified into two cases: 1) stationary and 2) nonstationary scenes.

For stationary scenes without along-track deformation (i.e., $\Delta\varepsilon_a = 0$), (28) becomes

$$\dot{\Phi}^{s1,s2} = k(\sigma_{M,S}(s1) - \sigma_{M,S}(s2)). \quad (29)$$

We can see that the differential phase $\dot{\Phi}$ is proportional to the derivative of the RME. The distance between the two looks is given as

$$\Delta x(R_0) = R_0(\tan\alpha_{s1} - \tan\alpha_{s2}). \quad (30)$$

From (29) and (30), the RME can be obtained by integrating the differential phase $\dot{\Phi}(x, R_0)$ as

$$\sigma_{M,S}(x, R_0) = \int_0^x \frac{\dot{\Phi}(x', R_0)}{k\Delta x(R_0)}dx' + \text{Constant} \quad (31)$$

where x indicates the along-track position. Equation (31) is identical to the result given in [13]. In other words, the multisquint technology can also be implemented using the BP algorithm to estimate RME.

For nonstationary scenes with along-track deformation (i.e., $\Delta\varepsilon_a \neq 0$), RME cannot be directly estimated from the integration of differential phase $\dot{\Phi}(x, R_0)$ because of the phase component caused by along-track deformation $\Delta\varepsilon_a$. One way to estimate RME for nonstationary scenes is to calculate the difference between two adjacent differential phases $\dot{\Phi}^{s1,s2}$ and $\dot{\Phi}^{s2,s3}$ as [28]

$$\ddot{\Phi} = \dot{\Phi}^{s1,s2} - \dot{\Phi}^{s2,s3} = k(\sigma_{M,S}(s1) - \sigma_{M,S}(s2)) - k(\sigma_{M,S}(s2) - \sigma_{M,S}(s3)) \quad (32)$$

where $s3$ denotes a third subaperture with effective squint angle $\alpha_{s3} = 2\alpha_{s2} - \alpha_{s1}$. The phase component caused by $\Delta\varepsilon_a$ can be canceled out by the double differential phase $\ddot{\Phi}$, which is the second derivative of the RME $\sigma_{M,S}$. Therefore, the RME for nonstationary scenes can be obtained by a two-step integration of $\ddot{\Phi}$ as

$$\sigma_{M,S}(x, R_0) = \int_0^x \int_0^{x_1'} \frac{\ddot{\Phi}(x_2', R_0)}{k\Delta x^2(R_0)}dx_2'dx_1' + \text{Constant}. \quad (33)$$

Because of the two-step integration, the RME becomes more sensitive to phase noise than the one-step integration given in (31).

A flowchart of the BP-based multisquint technique with three looks is shown in Fig. 4. First, using the BP algorithm, the aperture can be split into N_{Look} adjacent looks

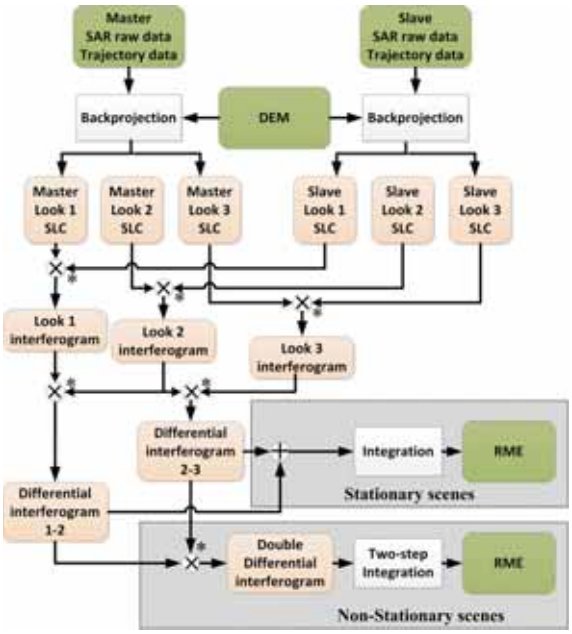

Fig. 4. Flowchart of estimating RME using the BP-based multisquint technique.

(e.g., $N_{\text{Look}} = 3$ in Fig. 4) and N_{Look} interferograms can be generated from corresponding looks of the Master and Slave data sets. Then $N_{\text{Look}} - 1$ differential interferograms can be obtained from the N_{Look} adjacent interferograms. For stationary scenes without along-track motion, RME can be estimated by integrating the combined $N_{\text{Look}} - 1$ differential interferograms. The combination of differential interferograms from different looks can reduce the noise, especially for low-coherence areas. For nonstationary scenes with along-track deformation, $N_{\text{Look}} - 2$ double differential interferogram can be generated from the phase difference of the adjacent differential interferograms. Finally, the RME can be estimated from a two-step integration.

It should be noted that the multisquint technique can only be used to estimate low frequency nonlinear RME. Globally constant and linear components of RME cannot be directly estimated in the integration procedure of the multisquint technique. One way to estimate the constant and linear RME is described in [11]: fitting the interferogram with a model and estimating the unknown parameters using weighted least squares estimation. For nonstationary scenes, the quadratic component of the RME should also be estimated from the fitted model. One key component of the multisquint technique is the bandwidth of the subaperture. A long subaperture cancels out RME with frequency higher than the subaperture's bandwidth [12]. In other words, multisquint techniques can only estimate the average of the true RME. The larger the subaperture, the less accurate the estimation of the high-frequency RME. However, if the subaperture is too short, the differential phases become noisy. It should be noted that three subapertures ($N_{\text{Look}} = 3$) are used in Fig. 4 for simplification. In practice, multiple looks can be used to estimate RME, such as $N_{\text{Look}} = 5$ in [14], $N_{\text{Look}} = 8$ in [17], and $N_{\text{Look}} = 9$ in [28]. As discussed in [14], the optimal

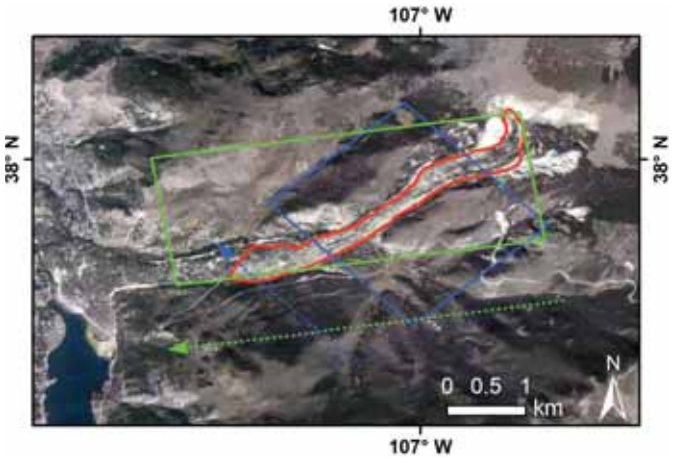

Fig. 5. Optical image of the Slumgullion landslide area from Google Earth with the red outline indicating the boundary of the active portion of the landslide. Two dotted arrows indicate two flight paths, one flown across the earthflow and one flown along the earthflow. The blue and green rectangles denote the corresponding coverage areas, respectively.

TABLE I
PARAMETERS OF THE SLIMSAR SYSTEM

Parameter Name	Values
Center Frequency	1.3075 GHz
Bandwidth	185 MHz
Chirp Time	1.555523 μs
Pulse Repetition Frequency (PRF)	1509.516 Hz
Altitude (above ground level)	~1066 m
Number of Antennas	2
Polarization	VV

number of looks and bandwidth depend on the coherence and magnitude of RME and should be selected on a case-by-case basis. In this paper, $N_{\text{Look}} = 6$ was used to estimate RME.

III. EXPERIMENTAL RESULTS

A. Study Area and Data

The Slumgullion landslide located in the San Juan Mountains near Lake City, CO, USA, is a long-term slow moving landslide that moves downhill continuously [29]–[31]. The "neck" of the landslide has the fastest speed of ~2 cm/day. An optical image of the Slumgullion landslide is shown in Fig. 5. In 2015, we conducted a pilot study over the Slumgullion landslide using an L-band airborne SAR system known as ARTEMIS SlimSAR, which is a compact, modular, and multifrequency radar system [3], [32]. The specifications of the SlimSAR system are summarized in Table I.

Two pairs of InSAR data are used to evaluate the performance of the proposed method for both stationary and nonstationary cases. As shown in Fig. 5, the blue dotted arrow indicates the flight path across the earthflow and the green dotted arrow indicates the flight path along the earthflow. The repeat-pass baselines for the across and parallel flights are shown in Fig. 6. The acquisition dates for the across

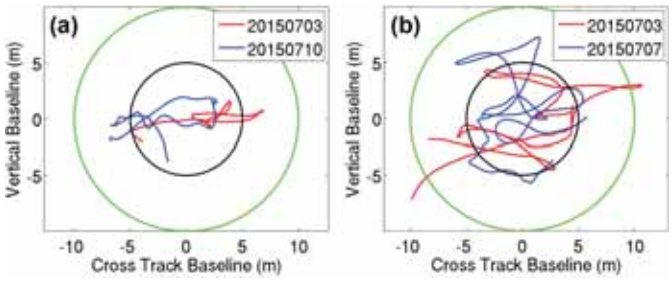

Fig. 6. Repeat-pass baselines for (a) across and (b) parallel flights, respectively. The deviations of the Master and Slave tracks are shown, within a 10-m tube (black circle) and 20-m tube (green circle). The baselines for approximately 75% of the flight lines are contained within the 10-m tube.

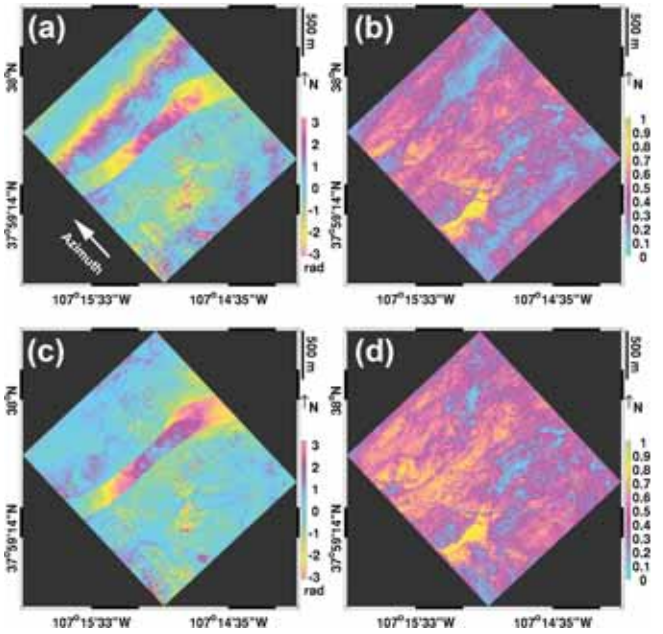

Fig. 7. Interferograms and coherence maps for the across path collections. (a) Initial interferogram. (b) Initial coherence. (c) Final interferogram after RME removal. (d) Final coherence after RME removal. All interferograms are wrapped and geocoded.

and parallel flights are 20150703-20150710 and 20150703-20150707, respectively. Since the across path were nearly perpendicular to the landslide motion direction, the along-track motion was assumed to be zero and RME could be estimated for a stationary scene case. On the other hand, the InSAR pair for the parallel flight lines should be evaluated as a nonstationary scene due to the landslide motion. Therefore, the across and parallel flights are used to verify RME removal for stationary and nonstationary scenes, respectively.

B. RME Removal for a Stationary Scene

For the across path, the initial interferogram and coherence generated using the full aperture are shown in Fig. 7(a) and (b), respectively. The movement of the landslide is clearly visible when compared with the nonmoving areas surrounding the slide. We observe that the surface displacement due to the landslide gradually increases from the bottom to the top. It is known that RME can result in a phase undulation in azimuth

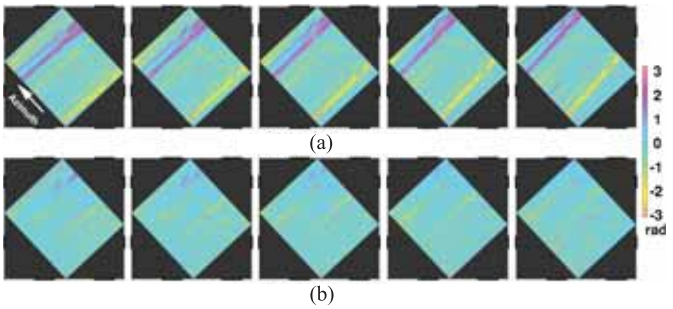

Fig. 8. Differential interferograms for the across path collections. (a) Initial differential interferograms before RME removal. (b) Final differential interferograms after RME removal.

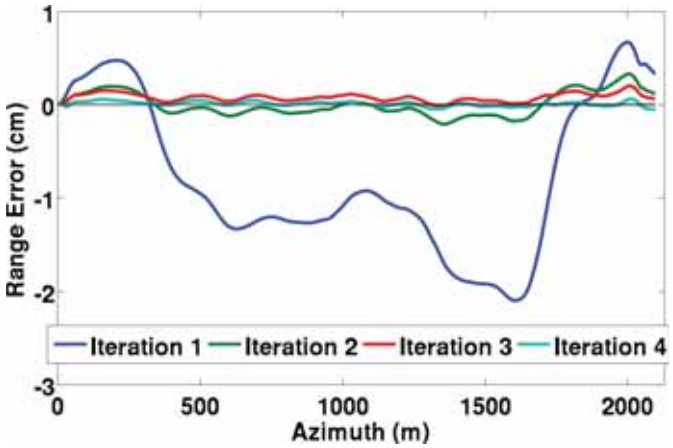

Fig. 9. Estimated residual baseline error in the LOS direction for the middle range for the across path collections.

direction [12], [13], which can be seen in Fig. 7(a). Such phase undulation can cause bias in the deformation estimate.

In order to remove the RME, six looks ($N_{\text{Look}} = 6$) with a bandwidth of 35 Hz each and with center equal to ± 8.75, ± 26.25, and ± 43.75 Hz were generated. In this case, the total used bandwidth is 122.5 Hz and split into six segments with overlap of 17.5 Hz. Then, five differential interferograms were obtained as shown in Fig. 8(a). The phase undulations in the azimuth direction caused by RME are immediately apparent. The RME can be estimated by integrating the combined differential interferometric phases along the azimuth direction. We estimated the RME by iteratively implementing the BP-based multisquint algorithm, as shown in Fig. 9. Since the RME is range-dependent, the estimated residual baseline error shown in Fig. 9 is for the midswath. We can see that the estimated RME was reduced from the maximum of 2.1 cm to less than 0.6 mm after four iterations. The five differential interferograms after removing RME are shown in Fig. 8(b), where the phase stripes have clearly been removed. We can use the standard deviation (STD) to measure the phase undulations. The averaged STD of the five differential interferogram was reduced from 0.85 to 0.5 rad after RME removal.

The final interferogram and coherence after removing RME are shown in Fig. 7(c) and (d), respectively. It can be seen from Fig. 7(c) that the phase undulation in the azimuth direction has been correctly removed. For nonlandslide area without motion, the STD of the interferogram has been reduced from

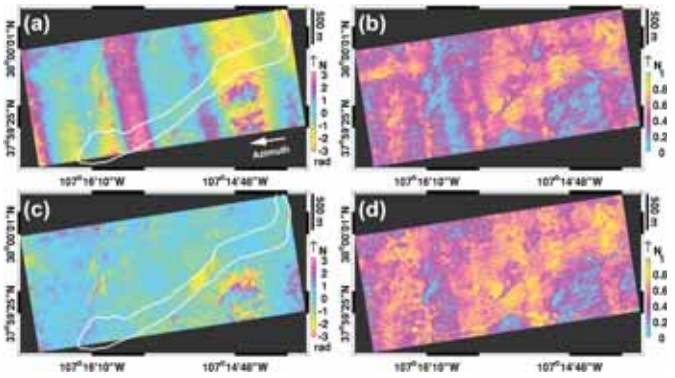

Fig. 10. Interferograms and coherence maps for the parallel path collections. (a) Initial interferogram. (b) Initial coherence. (c) Final interferogram after RME removal. (d) Final coherence after RME removal. All the interferograms are wrapped and geocoded. The white outlines in (a) and (c) indicate the boundary of the active portion of the landslide.

1.13 to 0.75 rad. Comparing Fig. 7(b) and (d), we can see that the coherence has been improved after removing RME, especially for the upper part of the image. The average coherence has improved from 0.38 to 0.45 after the RME removal. Therefore, we can see that the BP-based multisquint technique can successfully estimate the RME for stationary scenes.

C. RME Removal for Nonstationary Scenes

For the parallel path, the initial interferogram and coherence generated using the full aperture are shown in Fig. 10(a) and (b), respectively. We can see from Fig. 10(a) that the azimuth phase undulation is more severe than the across pair in Fig. 7(a), which indicates stronger RME.

Similar to the stationary case, six looks with a bandwidth of 35 Hz each and with center frequencies equal to ± 8.75, ± 26.25, and ± 43.75 Hz were generated. Five differential interferograms can also be obtained and are shown in Fig. 11(a). The phase stripes in the range direction caused by RME are clearly visible. Besides the phase component caused by the RME, the along-track landslide motion also induced phase components in the differential interferograms. Due to the small separation between two adjacent looks ($\sim 2.5°$), the effect of along-track motion is not clear in Fig. 11(a). Then, four double differential interferograms were generated as shown in Fig. 12(a). As expected, the double differential interferograms are noisier than the differential interferograms in Fig. 11(a). The RME can be estimated by a two-step integration of the combined double differential interferometric phases along the azimuth direction, as shown in Fig. 13. We can see that the estimated RME was reduced from a maximum of 3 cm to less than 1.2 mm after four iterations. The five differential interferograms and four double differential interferograms after removing RME are shown in Figs. 11(b) and 12(b), respectively. We can see that the stripes have been effectively reduced after RME correction. For nonlandslide area, the averaged STD of the five differential interferogram was reduced from 0.77 to 0.39 rad after RME removal. The averaged STD of the four double differential interferogram was reduced from 0.72 to 0.47 rad.

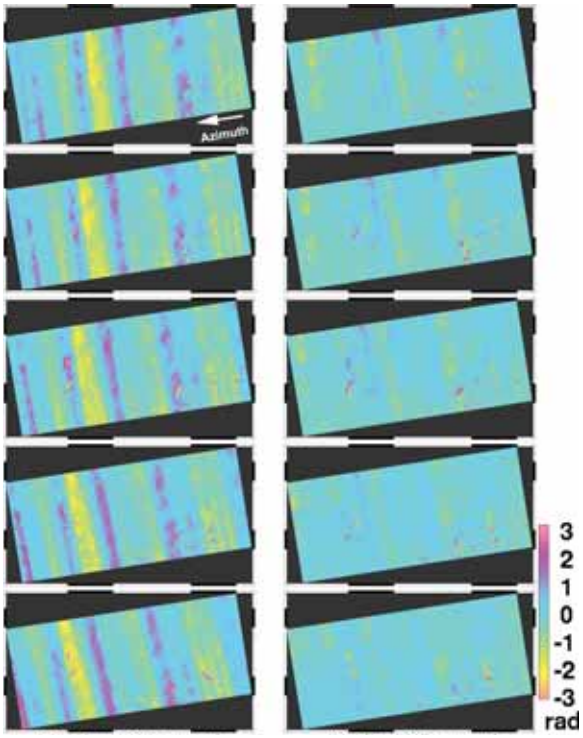

(a) (b)

Fig. 11. Differential interferograms for the parallel path collections. (a) Initial differential interferograms before RME removal. (b) Final differential interferograms after RME removal.

The final interferogram and coherence after RME removal are shown in Fig. 10(c) and (d), respectively. It can be seen from Fig. 10(c) that the phase undulation in the azimuth direction has been correctly removed. For nonlandslide, the STD of the interferogram has been reduced from 1.39 to 0.76 rad after RME removal. The phase noise shown in the lower-right part of Fig. 10(c) is caused by volume decorrelation due to vegetation. The average coherence has been improved from 0.44 to 0.51 after RME removal, as shown in Fig. 10(d). Therefore, we can see that the BP-based multisquint technique can also successfully estimate RME for nonstationary scenes.

The major limitation of the proposed method is the heavy computational burden of the BP algorithm. However, thanks to progress in computing technology, it can be easily mitigated by using alternate computing devices, such as a graphics processing unit (GPU). For example, in this paper, a desktop with a 1.8-GHz Quad Core CPU processor and two GeForce GTX TITAN X GPU devices were used to perform the BP focusing. For an SAR SLC image containing 4228×4404 pixels, the average processing time for BP focusing was 73 s. Therefore, the computational burden of the BP method was not a significant concern in this paper.

It should be noted that a conclusion about whether the proposed method outperforms the existing MoCo-based RME estimation methods is difficult to make due to the fact that a "well-designed" MoCo method can obtain similar results to BP [7], [12]. The motivation of this paper is to propose a method that is suitable for an SAR system mounted on a small aircraft toward promoting airborne InSAR applications. Because of its low altitude, it is expected that nonlinear flight tracks are more prevalent for the SlimSAR campaigns. Therefore, BP-based methods are more suitable for the SlimSAR system and can provide more flexibility in the future mission design. The study of BP-based RME estimation is needed for the successful application of small SAR systems, such as the SlimSAR system. Therefore, the comparison of the proposed and existing techniques is beyond the scope of this paper.

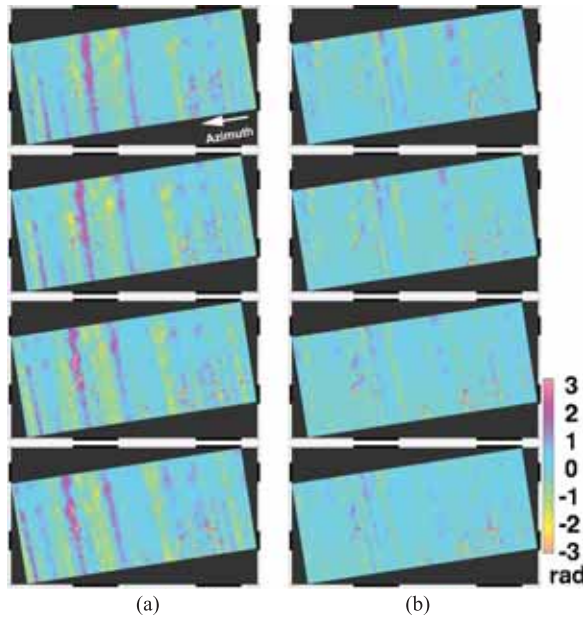

(a) (b)

Fig. 12. Double differential interferograms for the parallel path collections. (a) Initial double differential interferograms before RME removal. (b) Final double differential interferograms after RME removal.

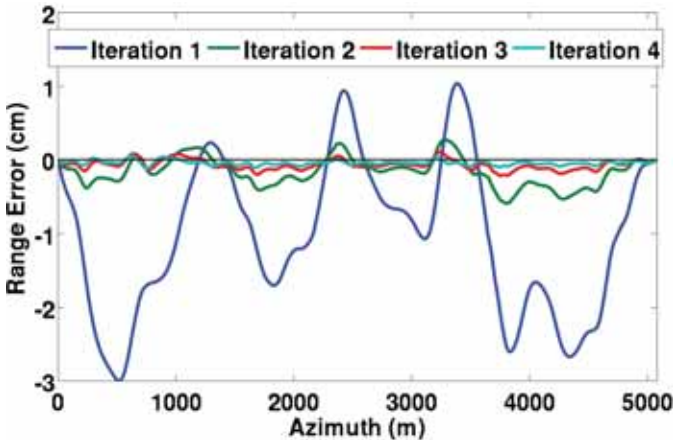

Fig. 13. Estimated residual baseline error in the LOS direction for the middle range for the parallel path collections.

IV. Conclusion

For the first time, this paper demonstrates the capability of using the BP-based multisquint technique to estimate RME. First, the signal properties of the BP algorithm are discussed to show how the BP algorithm focuses the SAR image with a nonlinear trajectory. It has been shown that both pixel-dependent MoCo and aperture-dependent MoCo are inherently taken into account in the BP algorithm. Then, the effect

of RME on the focused image is discussed and details for implementing the multisquint technique based on BP is given. Experimental results acquired over the Slumgullion landslide area by the SlimSAR system demonstrated that the proposed BP-based multisquint technique has the potential to reduce the RME for both stationary and nonstationary cases. In the long run, the proposed method can be a complement to existing methods to estimate RME and acquire reliable surface deformation from airborne InSAR data.

ACKNOWLEDGMENT

The authors would like to thank the two anonymous reviewers for their valuable suggestions and comments.

REFERENCES

[1] D. Massonnet and K. L. Feigl, "Radar interferometry and its application to changes in the Earth's surface," *Rev. Geophys.*, vol. 36, no. 4, pp. 441–500, Nov. 1998.
[2] Z. Lu, and D. Dzurisin, *InSAR Imaging of Aleutian Volcanoes: Monitoring a Volcanic Arc from Space* (Geophysical Sciences). Berlin, Germany: Springer, 2014.
[3] E. Zaugg, M. Edwards, and A. Margulis, "The SlimSAR: A small, multifrequency, synthetic aperture radar for UAS operation," in *Proc. IEEE Radar Conf.*, May 2010, pp. 277–282.
[4] A. Reigber and R. Scheiber, "Airborne differential SAR interferometry: First results at L-band," *IEEE Trans. Geosci. Remote Sens.*, vol. 41, no. 6, pp. 1516–1520, Jun. 2003.
[5] S. Hensley, H. Zebker, C. Jones, T. Michel, R. Muellerschoen, and B. Chapman, "First deformation results using the NASA/JPL UAVSAR instrument," in *Proc. 2nd Asian–Pacific Conf. Synth. Aperture Radar*, Oct. 2009, pp. 1051–1055.
[6] S. Perna, C. Wimmer, J. Moreira, and G. Fornaro, "X-band airborne differential interferometry: Results of the OrbiSAR campaign over the Perugia area," *IEEE Trans. Geosci. Remote Sens.*, vol. 46, no. 2, pp. 489–503, Feb. 2008.
[7] A. Moreira and Y. Huang, "Airborne SAR processing of highly squinted data using a chirp scaling approach with integrated motion compensation," *IEEE Trans. Geosci. Remote Sens.*, vol. 32, no. 5, pp. 1029–1040, Sep. 1994.
[8] P. Prats, A. Reigber, and J. J. Mallorqui, "Topography-dependent motion compensation for repeat-pass interferometric SAR systems," *IEEE Geosci. Remote Sens. Lett.*, vol. 2, no. 2, pp. 206–210, Apr. 2005.
[9] K. A. C. de Macedo and R. Scheiber, "Precise topography- and aperture-dependent motion compensation for airborne SAR," *IEEE Geosci. Remote Sens. Lett.*, vol. 2, no. 2, pp. 172–176, Apr. 2005.
[10] G. Fornaro, G. Franceschetti, and S. Perna, "Motion compensation errors: Effects on the accuracy of airborne SAR images," *IEEE Trans. Aerosp. Electron. Syst.*, vol. 41, no. 4, pp. 1338–1352, Oct. 2005.
[11] P. Prats, K. A. C. de Macedo, A. Reigber, R. Scheiber, and J. J. Mallorqui, "Comparison of topography- and aperture-dependent motion compensation algorithms for airborne SAR," *IEEE Geosci. Remote Sens. Lett.*, vol. 4, no. 3, pp. 349–353, Jul. 2007.
[12] A. Reigber, "Correction of residual motion errors in airborne SAR interferometry," *Electron. Lett.*, vol. 37, no. 17, pp. 1083–1084, Aug. 2001.
[13] P. Prats and J. J. Mallorqui, "Estimation of azimuth phase undulations with multisquint processing in airborne interferometric SAR images," *IEEE Trans. Geosci. Remote Sens.*, vol. 41, no. 6, pp. 1530–1533, Jun. 2003.
[14] A. Reigber, P. Prats, and J. J. Mallorqui, "Refined estimation of time-varying baseline errors in airborne SAR interferometry," *IEEE Trans. Geosci. Remote Sens.*, vol. 3, no. 1, pp. 145–149, Jan. 2006.
[15] A. Reigber *et al.*, "Very-high-resolution airborne synthetic aperture radar imaging: Signal processing and applications," *Proc. IEEE*, vol. 101, no. 3, pp. 759–783, Mar. 2013.
[16] S. Hensley *et al.*, "Residual motion estimation for UAVSAR: Implications of an electronically scanned array," in *Proc. Radar Conf.*, Pasadena, CA, USA, May 2009, pp. 1–5.
[17] K. A. C. D. Macedo, R. Scheiber, and A. Moreira, "An autofocus approach for residual motion errors with application to airborne repeat-pass SAR interferometry," *IEEE Trans. Geosci. Remote Sens.*, vol. 46, no. 10, pp. 3151–3162, Oct. 2008.
[18] G. Fornaro, G. Franceschetti, and S. Perna, "On center-beam approximation in SAR motion compensation," *IEEE Geosci. Remote Sens. Lett.*, vol. 3, no. 2, pp. 276–280, Apr. 2006.
[19] M. Soumekh, *Synthetic Aperture Radar Signal Processing: With MATLAB Algorithms*. Hoboken, NJ, USA: Wiley, 1999.
[20] J. C. Curlander and R. N. McDonough, *Synthetic Aperture Radar: Systems and Signal Processing*. Hoboken, NJ, USA: Wiley, 1991.
[21] A. F. Yegulalp, "Fast backprojection algorithm for synthetic aperture radar," in *Proc. Rec. IEEE Radar Conf.*, Apr. 1999, pp. 60–65.
[22] L. M. H. Ulander, H. Hellsten, and G. Stenstrom, "Synthetic-aperture radar processing using fast factorized back-projection," *IEEE Trans. Aerosp. Electron. Syst.*, vol. 39, no. 3, pp. 760–776, Jul. 2003.
[23] O. Frey, C. Magnard, M. Rüegg, and E. Meier, "Focusing of airborne synthetic aperture radar data from highly nonlinear flight tracks," *IEEE Trans. Geosci. Remote Sens.*, vol. 47, no. 6, pp. 1844–1858, Jun. 2009.
[24] M. I. Duersch and D. G. Long, "Analysis of time-domain back-projection for stripmap SAR," *Int. J. Remote Sens.*, vol. 36, no. 8, pp. 2010–2036, Apr. 2015, doi: 10.1080/01431161.2015.1030044.
[25] O. Frey, E. Meier, and D. Nüesch, "A study on integrated SAR processing and geocoding by means of time-domain backprojection," in *Proc. Int. Radar Symp.*, Berlin, Germany, 2005, pp. 1–5.
[26] S. Buckreuss, "Motion errors in an airborne synthetic aperture radar system," *Trans. Emerg. Telecommun. Technol.*, vol. 2, no. 6, pp. 655–664, Nov./Dec. 1991.
[27] H. A. Zebker and J. Villasenor, "Decorrelation in interferometric radar echoes," *IEEE Trans. Geosci. Remote Sens.*, vol. 30, no. 5, pp. 950–959, Sep. 1992.
[28] P. Prats, R. Scheiber, A. Reigber, C. Andres, and R. Horn, "Estimation of the surface velocity field of the Aletsch glacier using multibaseline airborne SAR interferometry," *IEEE Trans. Geosci. Remote Sens.*, vol. 47, no. 2, pp. 419–430, Feb. 2009.
[29] M. Parise and R. Guzzi, "Volume and shape of the active and inactive parts of the Slumgullion landslide, Hinsdale County, Colorado," U.S. Geol. Survey, Reston, VA, USA, Tech. Rep. 92–216, 1992, p. 29.
[30] D. J. Varnes and W. Z. Savage, "The Slumgullion earth flow; a large-scale natural laboratory," U.S. Geol. Survey Bull., Washington, DC, USA, Tech. Rep. 2130, 1996, p. 95.
[31] R. W. Fleming, R. L. Baum, and M. Giardino, "Map and description of the active part of the Slumgullion landslide, Hinsdale County, Colorado," in *U.S. Geological Survey Geologic Investigations Series Map I-2672*. Denver, CO, USA: U.S. Geological Survey, 1999, p. 34.
[32] N. Cao *et al.*, "Airborne DInSAR results using time-domain back-projection algorithm: A case study over the Slumgullion landslide in Colorado with validation using spaceborne SAR, airborne LiDAR, and ground-based observations," *IEEE J. Sel. Topics Appl. Earth Observ. Remote Sens.*, vol. 10, no. 11, pp. 4987–5000, Nov. 2017, doi: 10.1109/JSTARS.2017.2737362.

Ning Cao received the B.S. and M.S. degrees in electronic engineering from the Harbin Institute of Technology, Harbin, China, in 2011 and 2013, respectively, and the Ph.D. degree in geosensing systems engineering and sciences from the Department of Civil and Environmental Engineering, University of Houston, Houston, TX, USA, in 2016.

He currently holds a post-doctoral position at the Department of Civil and Environmental Engineering and the National Center for Airborne Laser Mapping, University of Houston. His research interests include multitemporal interferometric synthetic aperture radar (SAR) techniques and airborne SAR/SAR interferometry.

Hyongki Lee received the Ph.D. degree in geodetic science from The Ohio State University, Columbus, OH, USA, in 2008.

He is currently an Associate Professor with the Department of Civil and Environmental Engineering, University of Houston, Houston, TX, USA. His research interests include using spaceborne and airborne geodetic instruments for earth science problems.

Dr. Lee is a recipient of the National Aeronautics and Space Administration New Investigator Award in earth science in 2014.

Evan Zaugg received the B.S. and Ph.D. degrees in electrical engineering from Brigham Young University, Provo, UT, USA, in 2005 and 2010, respectively.

He is currently with ARTEMIS, Inc., Hauppauge, NY, USA, where he is involved in the research and development of synthetic aperture radar (SAR) systems, data processing, and exploitation, including advanced SAR image formation algorithms, ground moving target indicators, interferometry, and change detection.

Ramesh Shrestha received the Ph.D. degree from the University of Wisconsin–Madison, Madison, WI, USA.

He is currently a Hugh Roy and Lillie Cranz Cullen University Professor with the University of Houston (UH), Houston, TX, USA, where he leads the geosensing systems engineering graduate research and academic programs and is also a Principal Investigator and the Director of the National Science Foundation funded National Center for Airborne Laser Mapping, which is jointly operated by UH and the University of California at Berkeley, Berkeley, CA, USA. His research interests include the application of advanced geodetic and remote-sensing techniques, particularly airborne laser swath mapping (also known as light detection and ranging) and digital mapping.

William E. (Bill) Carter received the Ph.D. degree from the University of Arizona, Tucson, AZ, USA, where he was part of a team that developed one of the first lunar laser ranging observatories.

He spent 20 years with the National Geodetic Survey, National Oceanic and Atmospheric Administration, Silver Spring, MD, USA, followed by 14 years as an Adjunct Professor and a Senior Researcher at the University of Florida, Gainesville, FL, USA, where he was involved in geodetic imaging. He is currently a Research Professor with the Department of Civil and Environmental Engineering, University of Houston, Houston, TX, USA.

Craig Glennie received the B.Sc. and Ph.D. degrees in geomatics engineering from the University of Calgary, Calgary, AB, Canada.

He was a Vice President of Engineering for Terra Point, Lakeway, TX, USA, a light detection and ranging remote-sensing company with offices in Canada and USA. He has been active in the design, development, and operation of kinematic remote sensing systems for 18 years. He is currently an Associate Professor in civil and environmental engineering with the University of Houston, Houston, TX, USA, where he is also a Co-Principal Investigator with the National Science Foundation funded National Center for Airborne Laser Mapping. He is also a registered Professional Engineer in Alberta, Canada.

Zhong Lu received the B.S. and M.S. degrees from Peking University, Beijing, China, in 1989 and 1992, respectively, and the Ph.D. degree from the University of Alaska Fairbanks, Fairbanks, AK, USA, in 1996.

He was a Physical Scientist with the United States Geological Survey (USGS), Reston, VA, USA, from 1997 to 2013. He is currently a Professor and an endowed Shuler-Foscue Chair with the Roy M. Huffington Department of Earth Sciences, Southern Methodist University, Dallas, TX, USA. He is also a Principal Investigator of projects funded by the National Aeronautics and Space Administration (NASA), the European Space Agency, the Japan Aerospace Exploration Agency, the German Aerospace Center, and USGS for the study on land surface deformation using satellite synthetic aperture radar interferometry (InSAR) imagery. He has authored over 45 and co-authored over 105 peer-reviewed journal articles and book chapters focused on InSAR techniques and applications. He has co-authored the book *InSAR Imaging of Aleutian Volcanoes: Monitoring a Volcanic Arc From Space* (Springer, 2014). His research interests include the technique developments of SAR, InSAR, and persistent scatterer InSAR processing and their applications on volcanoes, landslides, and coastal processes among others.

Dr. Lu was a recipient of the Ford Senior Research Fellowship, the American Society for Photogrammetry and Remote Sensing Award for Best Scientific Paper in Remote Sensing, the NASA Group Achievement Award, an NASA Certificate of Appreciation, the Raytheon Distinguished Level Award for Excellence in Technology, the Science Applications International Corporation Technical Fellowship, and the Jerald Cook Memorial Award. He is a Committee Member of the Western North America InSAR Consortium, the NASA's Alaska Satellite Facility User Working Group, and the upcoming NASA-India SAR Science Definition Team. He is an Associate Editor of *Remote Sensing* and a member of the Editorial Board of the *International Journal of Image and Data Fusion* and the Editorial Board of *Geomatics, Natural Hazards and Risk*.

Hanwen Yu was born in Shaanxi, China, in 1985. He received the B.S. and Ph.D. degrees in electronic engineering from Xidian University, Xi'an, China, in 2007 and 2012, respectively, and the M.S. degree in computer science from the University of Memphis, Memphis, TN, USA, in 2015.

He is currently a Post-Doctoral Research Fellow with the Department of Civil and Environmental Engineering and the National Center for Airborne Laser Mapping, University of Houston, Houston, TX, USA. His research interests include phase unwrapping, algorithm design, and synthetic aperture radar interferometry signal processing and application.